AMSR2

SEA ICE ALGORITHM THEORETICAL BASIS DOCUMENT

Walter N. Meier

Thorsten Markus

Josefino Comiso

Alvaro Ivanoff

Jeffrey Miller

NASA Goddard Space Flight Center

Cryospheric Sciences Lab

Code 615

Greenbelt, MD 20771

12 July 2017

Table of Contents

1. Overview

The AMSR2 sea ice standard level 3 products include sea ice concentration, snow depth on sea ice, and sea ice drift. It is similar to the AMSR-E products, with adjustments for the change in sensor. Much of the content here is adapted from the AMSR-E ATBD. The AMSR2 standard sea ice concentration product is generated using the enhanced NASA Team (NT2) algorithm described by Markus and Cavalieri (2000, 2009), the snow depth is produced from the algorithm described by Markus and Cavalieri (1998) for both hemispheres, but excluding the Arctic perennial ice regions, and the sea ice drift is produced from an algorithm described by Liu and Cavalieri (1998). Additionally, the difference between the AMSR2 Bootstrap (ABA) and the NT2 retrieved concentrations (ABA-NT2) are archived. These products together with AMSR2 calibrated brightness temperatures (TBs) are mapped to the same polar stereographic projection used for SSMI data to provide the research community consistency and continuity with the existing 32-year Nimbus 7 SMMR and DMSP SSMI sea ice concentration products. The TB grid resolutions are as follows: (a) TBs for all AMSR2 channels: 25-km, (b) TBs for the 18, 23, 36, and 89 GHz channels: 12.5-km, (c) TBs for the 89 GHz channels: 6.25-km. All of these TB products are stored as a composite of (i) daily-averaged ascending orbits only, (ii) daily-averaged descending orbits only, and (iii) all orbits creating a full daily average. Sea ice concentrations are produced at 12.5-km and 25-km resolutions and stored as a composite of daily-averaged ascending orbits, daily-averaged descending orbits, and all orbits for a full daily average, similar to the TB products. Snow depth on sea ice is produced as a 5-day average at a resolution of 12.5 km. Sea ice drift is also a five-day product computed at a resolution of 6.25-km, but mapped at a resolution of 100-km.

The algorithms described below are essentially the same as those developed for AMSR-E. The primary change for AMSR2 is an adjustment to the AMSR2 brightness temperatures to be consistent with the AMSR-E values. This adjustment is summarized in Section 3.2.4

2. Background

2.1 Experimental objective

The objective of the AMSR2 sea ice products is to provide high-quality estimates of important geophysical sea ice parameters, including: concentration, snow depth on sea ice, and drift. These fields will continue the time series that began with AMSR-E in 2002. With the addition of calibrated AMSR2 parameters, the AMSR (including both AMSR-E and AMSR2) will extent at least 15 years, providing a higher quality complement to the long-term nearly 40-year record of passive microwave sea ice estimates from SMMR, SSMI, and SSMIS.

2.2 Historical prospective

Sea ice is a key climate indicator due to its high albedo that reflects incoming solar radiation, its role as a physical barrier to heat and moisture transfer between the ocean and atmosphere, and

its role in biogeochemical cycles. It is also plays a major role in polar ecosystems and in lives of indigenous peoples of the Arctic. Changes in Arctic sea ice over the past nearly four decades have been dramatic, with a loss of over a third of summer ice cover, a large decline in ice thickness, and a nearly-complete loss of old ice. Satellite remote sensing has been the primary tool for mapping sea ice concentration, extent, and age since the late 1970s. The consistent and continuous long-term multichannel microwave radiometer sea ice record began in October 1978 with the Scanning Multichannel Microwave Radiometer (SMMR) on the NASA Nimbus-5 satellite, followed by a series of Special Sensor Microwave Imagers (SSMI) and Special Sensor Microwave Imager/Sounders (SSMIS) instruments on U.S. Defense Meteorological Satellite Program (DMSP) platforms. The SSMI and SSMIS record began in July 1987 and continues today (through mid-2017). These sensors provide the continuous and consistent long-term record of sea ice that is now nearly 40 years long. Starting in 2002, the Advanced Microwave Scanning Radiometer for the Earth Observing System (AMSR-E), a JAXA sensor launched on the NASA Aqua satellite, provides improved spatial resolution and other advances over the SMMR-SSMI-SSMIS record. The Advanced Microwave Sounding Radiometer 2 (AMSR2) onboard the first Global Change Observation Mission – Water (GCOM-W1) satellite includes similar characteristics as AMSR-E with slightly better spatial resolution and other improvements. The AMSR-E and AMSR2 sensor provide a 15+ year record of enhanced sea ice retrievals that complement the longer record.

3. Theoretical Basis of Algorithm

3.1 Physics of the problem

Passive microwave radiation is naturally emitted by the Earth's surface and overlying atmosphere. This emission is a complex function of the microwave radiative properties of the emitting body (Hallikainen and Winebrenner, 1992). However, for the purposes of microwave remote sensing, the relationship can be described as a simple function of the physical temperature (T) of the emitting body and the emissivity (ε) of the body.

$$T_B = \varepsilon * T \qquad (1)$$

T_B is the brightness temperature and is the parameter (after calibrations) retrieved by satellite sensors and is the input parameter to passive microwave sea ice concentration algorithms.

The microwave electromagnetic properties of sea ice are a function of the physical properties of the ice, such as crystal structure, salinity, temperature, or snow cover. In addition, open water typically has an electromagnetic emission signature that is distinct from sea ice emission (Eppler et al., 1992). These properties form the basis for passive microwave retrieval of sea ice concentrations.

Specifically, the unfrozen water surface is highly reflective in much of the microwave regime, resulting in low emission (Figure 5). In addition, emission from liquid water is highly polarized.

When salt water initially freezes into first-year (FY) ice (ice that has formed since the end of the previous melt season), the microwave emission changes substantially; the surface emission increases and is only weakly polarized. Over time as freezing continues, brine pockets within the sea ice drain, particularly if the sea ice survives a summer melt season when much of the brine is flushed by melt water. This multi-year (MY) ice has a more complex signature with characteristics generally between water and first-year ice. Other surface features can modify the microwave emission, particularly snow cover, which can scatter the ice surface emission and/or emit radiation from within the snow pack. Atmospheric emission also contributes to any signal received by a satellite sensor. These issues result in uncertainties in the retrieved concentrations, which are discussed further below.

Because of the complexities of the sea ice surface as well as surface and atmospheric emission and scattering, direct physical relationships between the microwave emission and the physical sea ice concentration are not feasible. Thus, the standard approach is to derive concentration through empirical relationships. These empirically-derived algorithms take advantage of the fact that brightness temperature in microwave frequencies tend to cluster around consistent values for pure surface types (100% water or 100% sea ice). Concentration can then be derived using a simple linear mixing equation (Zwally et al., 1983) for any brightness temperature that falls between the two pure surface values:

$$T_B = T_I C_I + T_O(1-C_I) \qquad (2)$$

Where T_B is the observed brightness temperature, T_I is the brightness temperature for 100% sea ice, T_O is the brightness temperature for open water, and C_I is the sea ice concentration.

In reality, such an approach is limited by the surface ambiguities and atmospheric emission. Using combinations of more than one frequency and polarization limits these effects, resulting in better discrimination between water and different ice types and a more accurate concentration estimate.

3.2 Mathematical description

3.2.1 Sea ice concentration

The two ratios of brightness temperatures used in the original NASA Team algorithm (Cavalieri et al. 1984; Gloersen and Cavalieri 1986; Cavalieri et al. 1995) as well as in the NT2 approach are the polarization

$$PR(v) = [TB(vV) - TB(v)] / [TB(vV) + TB(vH)] \qquad (3)$$

and the spectral gradient ratio

$$GR(v1pv2p) = TB(v1p) - TB(v2p)] / [TB(v1p) + TB(v2p)] \qquad (4)$$

where TB is the brightness temperature at frequency v for the polarized component p (vertical (V) or horizontal (H)).

Figure 1 (top) shows a typical scatterplot of PR(19) versus GR(37V19V) for September conditions in the Weddell Sea. The NT algorithm identifies two ice types that are associated with first-year and multiyear ice in the Arctic and ice types A and B in the Antarctic (as shown in Figure 1 (top)). The A-B line represents 100% ice concentration. The distance from the open water point (OW) to line A-B is a measure of the ice concentration. In this algorithm, the primary source of error is attributed to conditions in the surface layer such as surface glaze and layering (Comiso et al. 1997), which can significantly affect the horizontally polarized 19 GHz brightness temperature (Matzler et al. 1984) leading to increased PR(19) values and thus an underestimate of ice concentration. In the following discussion, we will refer to these effects as surface effects. In Figure 1 (top), pixels with significant surface effects tend to cluster as a cloud of points (labeled C) away from the 100% ice concentration line A-B resulting in an underestimate of ice concentration by the NT algorithm. The use of horizontally polarized channels makes it imperative to resolve a third ice type to overcome the difficulty of surface effects on the emissivity of the horizontally polarized component of the brightness temperature.

We make use of GR(89V19V) and GR(89H19H) to resolve the ambiguity between pixels with true low ice concentration and pixels with significant surface effects. A plot of these two ratios are found to form narrow clusters except for areas where surface effects decrease TB(19H) and consequently increase GR(89H19H) (Figure 1 (bottom)). Values of high GR(89V19V) and high GR(89H19H) are indicative of open water. The range of GR(89H19H) values is larger because of the greater dynamic range between ice and water for the horizontally polarized components. With increasing ice concentration, the two ratios have more similar values. The narrow cluster of pixels adjacent to the diagonal shown in Figure 1 (bottom) represents 100% ice concentration with different GR values corresponding to different ice types. When surface effects come into play, points deviate from this narrow cluster towards increased GR(89H19H) values (cloud of points to the right of the diagonal) while GR(89V19V) changes little or remains constant. This cloud of points labeled C in Figure 3 (bottom) also corresponds to the cluster of points labeled C in Figure 3 (top). The difference, therefore, between these two GRs (ΔGR) is used as a measure of the magnitude of surface effects. Based on this analysis we introduce a new ice type C, which represents ice having significant surface effects. For computational reasons we rotate the axes in PR-GR space (Figure 1 (top)) by an angle ϕ so the A-B line is vertical. This makes the rotated PRs ($PR_R(19)$ and $PR_R(89)$) independent of ice types A and B (first-year and multiyear for the Arctic). The use of the 89 GHz data requires a correction for atmospheric effects. This is accomplished through an additional AMSR2 variable, PR(89).

The response of the brightness temperatures to different weather conditions is calculated using an atmospheric radiative transfer model (Kummerow 1993). Input data into the model are the emissivities of first-year sea ice under winter conditions taken from Eppler et al. (1992) with

modifications to achieve agreement between modeled and observed ratios. Atmospheric profiles used as another independent variable in the algorithm, having different cloud properties, specifically cloud base, cloud top, cloud liquid water are taken from Fraser et al. (1975) and average atmospheric temperatures and humidity profiles for summer and winter conditions are taken from Antarctic research stations. These atmospheric profiles are based on climatology and are assumed valid for both hemispheres.

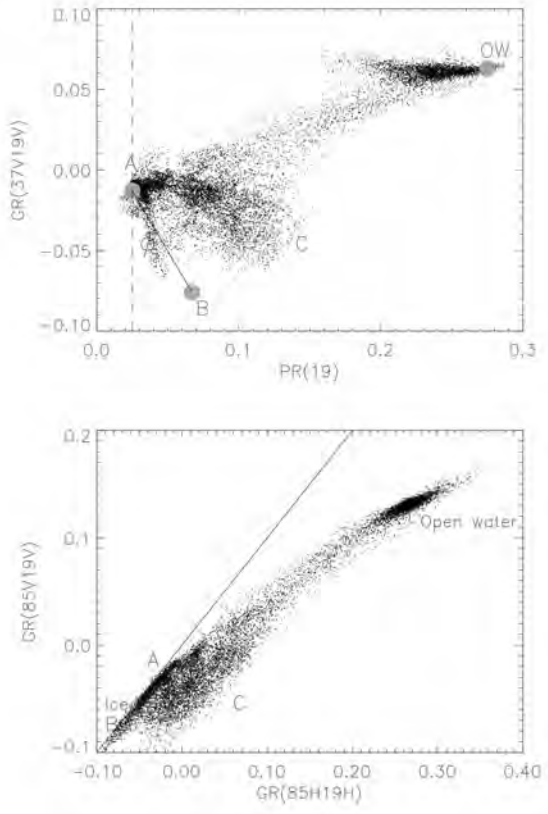

Figure 1: Top: GR(37V 19V) versus PR(19) for the Weddell Sea on September 15, 1992. The gray circles represent the tiepoints for the ice types A and B as well as for open water as used by the NT algorithm. Label C indicates pixels with significant surface effects. Φ is the angle between the y-axis and the A-B line. Bottom: GR(85V 19V) versus GR(85H19H). The ice types A and B are close to the diagonal. The amount of layering corresponds to the horizontal deviation from this line towards label C. Taken from Markus and Cavalieri [2000].

The plots of ΔGR versus PR_R (19) (Figure 2a) and ΔGR versus PR_R(89) (Figure 2b) illustrate the algorithm domain. The gray symbols indicate the tie-points with the different atmospheres for the three surface types (A, C, and OW). They also illustrate that the effect of weather is well modeled. For example, the cluster of open water values is mainly the result of changing atmospheric conditions. The modeled atmospheres adequately span the lengths of the OW clusters. A comparison of Figures B4a and B4b also shows how much more the 89 GHz data are affected by the atmosphere compared to the 19 GHz data.

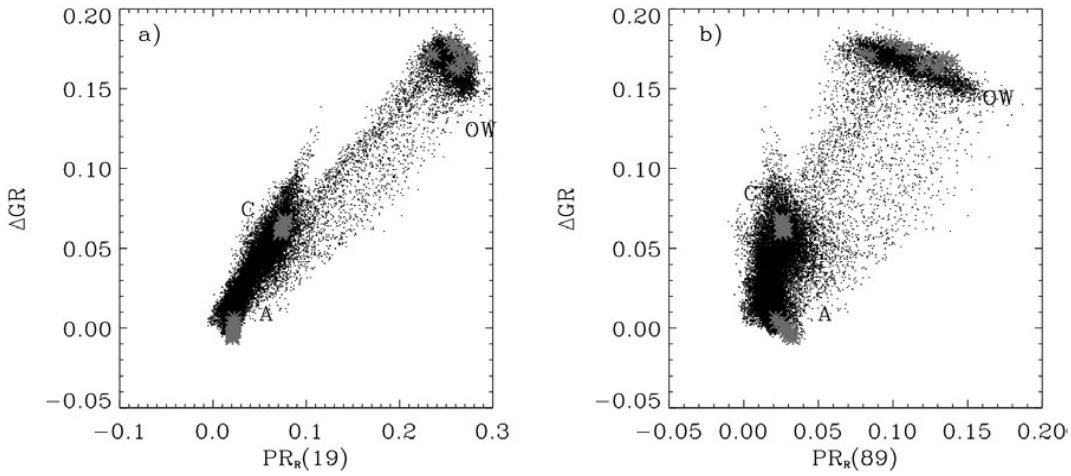

Figure 2 (a) ΔGR versus PRR (19) and (b) ΔGR versus PRR(89) for September 15, 2008. The gray symbols represent the NT2 tie

We, then, calculate brightness temperatures for all possible ice concentration combinations in 1% increments and for each of those solutions calculate the ratios PR_R (19), PR_R (89), and ΔGR. This creates a prism in which each element contains a vector with the three ratios (Figure 3). For each AMSR2 pixel PR_R (19), PR_R (89), and ΔGR are calculated from the observed brightness temperatures. Next, we move through this prism comparing the observed three ratios with the modeled ones. The indices where the differences are smallest will determine the final ice concentration combination and weather index. The next section will provide detailed information about the implementation.

Because of the unique signature of new ice in the microwave range, we solve for new ice instead of ice type C for selected pixels. Using a GR(37V19V) threshold of –0.02 we either resolve ice type C (for pixels where GR(37V19V) is below this threshold) or thin ice (for pixels where GR(37V19V) is above this threshold). Areas of ice type C and thin ice are mutually exclusive because thin ice has little, if any, snow cover. A limitation, of course, is that we cannot resolve mixtures of thin ice and thicker ice with layering in its snow cover.

3.2.1.1 Implementation of the concentration algorithm

In contrast to other operational sea ice concentration algorithms using daily averaged brightness temperatures as input, the AMSR-E NT2 concentrations are calculated from individual swath (Level 2) data from which daily maps are made by averaging these swath ice concentrations. Using swath brightness temperatures is particularly critical for the NT2 algorithm and its atmospheric correction. The atmospheric influence on the brightness

temperatures is non linear and by using average brightness temperatures we would dilute the atmospheric signal. The ice concentration algorithm is implemented as follows:

1. Generate look-up tables: For each AMSR channel with frequency v and polarization p calculate brightness temperature for each ice concentration-weather combination (using TBow, TBA/FY , TBC/thin as given in the Appendix of Markus and Cavalieri (2009)):

$$TB_{ca,cc,wx}(v\ p) = (1 - CA - CC) \bullet TB_{ow}(vpWx) + CA \bullet TB_{A/FY}(vpWx) + CC \bullet TB_{C/thin}(vpWx) \qquad (5)$$

where CA refers to the ice type A/B concentration (FY/MY for Arctic), CC to ice type C concentration, and Wx to the weather index. Ice concentrations are between 0 and 100 in 1% increments, weather indices are between 1 and 12 corresponding to the tables in the Appendix of Markus and Cavalieri (2009).

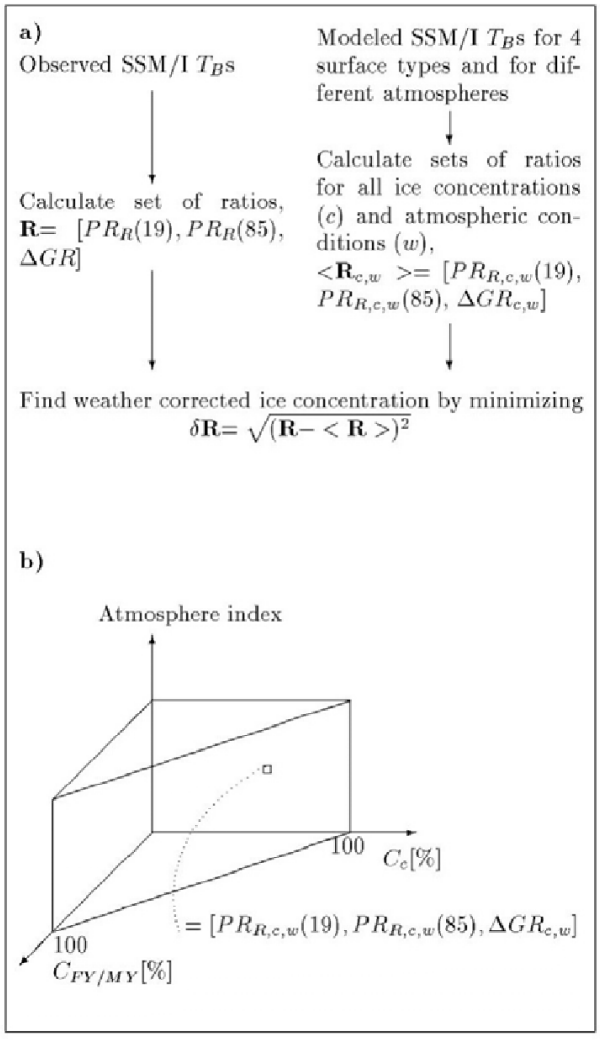

Figure 3. Flow diagram of the NT2 algorithm (from Markus and Dokken 2002).

2. From these TBs calculate ratios creating the look---up tables, e.g. LUT PR19(CA,CC,Wx) etc.:

LUT PR19(CA,CC,Wx) = [TBca,cc,wx(37V) − TBca,cc,wx(19V)] x sinϕ19 / [TBca,cc,wx(37V) + TBca,cc,wx(19V)] + [TBca,cc,wx(19V) − TBca,cc,wx(19H)] x cosϕ19 / [TBca,cc,wx(19V) + TBca,cc,wx(19H)] (6)

LUTPR89(ca, cc,wx) = [TBca,cc,wx(37V) − TBca,cc,wx(19V)] x sinϕ89 TBca,cc,wx(37V) + TBca,cc,wx(19V) + [TBca,cc,wx(89V) − TBca,cc,wx(89H)] x cosϕ89 / [TBca,cc,wx(89V) + TBca,cc,wx(89H)] (7)

If GR(37V19V) < -0.02 we solve for ice type C using ΔGR as our third variable, i.e.,

LUTdGR(ca, cc,wx) = [TBca,cc,wx(89H) − TBca,cc,wx(19H)] / [TBca,cc,wx(89H) + TBca,cc,wx(19H)] − [TBca,cc,wx(89V) − TBca,cc,wx(19V)] / [TBca,cc,wx(89V) + TBca,cc,wx(19V)] (8)

Whereas for pixels where GR(37V19V) > -0.02 we solve for thin ice using the standard GR(37V19V) as suggested by Cavalieri (1994), i.e.,

LUTdGR(ca, cc,wx) = [TBca,cc,wx(37V) − TBca,cc,wx(19V)]/[TBca,cc,wx(37V) + TBca,cc,wx(19V)] (9)

Each of these arrays has the dimensions of 101 x 101 x 12 where, of course, the total ice concentration (ca + cc) cannot exceed 100.

3. For each pixel i we have the actual measured AMSR-E brightness temperatures (TBi(νp))

4. Calculate same ratios from these brightness temperatures as in step 2 (PRi(19), etc.).

5. Compare these observed ratios with each of the ratios in the look-up tables looping through all ice concentration-weather combinations, i.e.,

$$\delta = (PRi(19) - LUTPR19(ca, cc,wx))^2 + (PRi(89) - LUTPR89(ca, cc,wx))^2 + (\Delta GRi - LUT\ dGR(ca, cc,wx))^2 \quad (10)$$

6. The indices ca, cc, wx where δ is minimal determine the ice concentration (and weather index), i.e.:

$$C_T = CA_{min}\delta + CC_{min}\delta \quad (11)$$

3.2.1.2 Land Spillover Correction

Although a land mask is applied to the ice concentration maps, land spillover still leads to erroneous ice concentrations along the coast lines adjacent to open water. This makes operational usage of these maps cumbersome. Therefore, we apply a land spillover correction scheme on the maps. The difficulty is to delete all clearly erroneous ice concentration while at the same time preserving actual ice concentrations, as for example, along the margins of coastal polynyas. We apply a five-step procedure.

1. Classify all pixels of the polar-stereographic grid with respect to the distance to coast. Ocean pixels directly along the coast are classified by 1, whereas pixels farther away are 2 and 3. Open ocean pixels are zero. Land pixels directly along the coast are classified as 4 and pixels farther away have increasing values.

2. All pixels with classes 1 or 2 will be assessed for erroneous sea ice concentrations due to land spillover by analyzing the 7 by 7 pixel neighborhood. The area of the neighborhood (7 pixels or 87.5 km) needs to be greater than the AMSR2 antenna pattern. Pixels with values of 3 and 0 will not be changed.

3. Check whether all class 3 pixels in 7-pixel neighborhood are open water (if so, set ice concentration to 0).

4. Calculate an average sea ice concentration for the 7 by 7 pixel box assuming all ocean pixels have zero ice concentration and all land pixels have an ice concentration of 90%. This approximates a theoretical concentration caused by land spillover only.

5. If the AMSR2 ice concentration is less than or equal to this value, set pixel at center of box to open water.

Figure 4 shows an example ice concentration with and without the land spillover correction.

3.2.1.3 Reduction of Atmospheric Effects

The NT2 algorithm has an atmospheric correction scheme as an inherent part of the algorithm. It provides weather-corrected sea ice concentrations through the utilization of a forward atmospheric radiative transfer (RT) model. However, to eliminate remaining severe weather effects over open ocean, two weather filters based on the spectral gradient ratio are implemented using threshold values similar to those used by the NT algorithm (Gloersen and Cavalieri 1986; Cavalieri et al. 1995). However, the advantage of the RT atmospheric correction is that not only are spurious ice concentrations over the open ocean removed, but atmospheric corrections are applied to ice covered portions of the ocean.

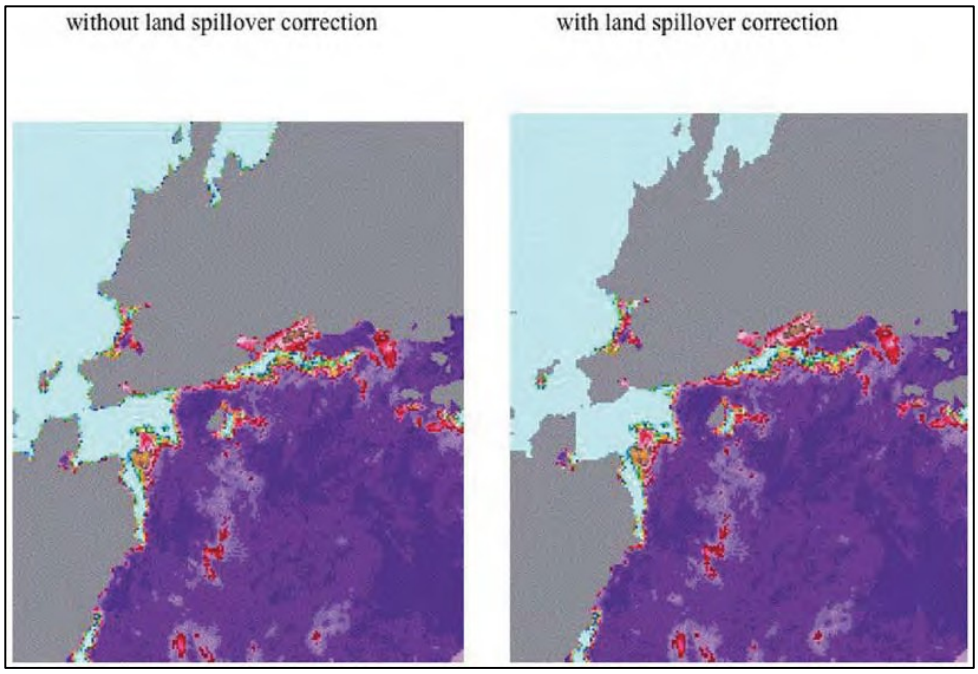

Figure 4. Map of ice concentration with and without land spillover correction.

Figure 5 shows AMSR-E sea ice concentration maps for the Sea of Okhotsk. Figure 5a shows the ice concentration map if PRR (19), PRR (89), and ΔGR are used without any weather correction. Figure 5b shows the ice concentration map with the NT2 weather correction. The differences between Figure 5a and 5b are shown in Figure 5d and illustrate the effect of the weather correction not only over the open ocean, but also over the sea ice. More severe weather effects over the open ocean (for example, in the bottom right corner) are finally removed by the NT weather filters (Figure 5c). The threshold for the GR(37V19V) NT weather filter (Gloersen and Cavalieri 1986) is 0.05, where the threshold for the GR(22V19V) NT weather filter (Cavalieri et al. 1995) is 0.045. If the respective GR values exceed these thresholds, the sea ice concentrations are set to zero. Figure 5e shows the difference in ice concentrations between the retrievals using only the NT2 weather correction and the retrievals using both the NT2 correction and the NT filters. A slight change along the ice edge is observed.

Even with both the atmospheric correction scheme and the GR filters, we still had problems with residual weather contamination particularly at low latitudes. A filter based on monthly climatological sea surface temperatures (SSTs) from the National Oceanic and Atmospheric Administration (NOAA) ocean atlas, used earlier by Cavalieri et al. (1999), was employed to eliminate these low-latitude spurious ice concentrations. In the Northern Hemisphere, any pixel where the monthly SST is greater than 278 K, the ice concentration is set to zero throughout the month; whereas in the Southern Hemisphere, wherever the monthly SST is greater than 275 K, the ice concentration is set to zero throughout the month. The higher SST threshold

value in the Northern Hemisphere is needed because the 275 K isotherm used in the Southern Hemisphere is too close to the ice edge in the north. The closest distance the threshold isotherms are to the ice edge is more than 400 km (Cavalieri et al. 1999).

In summary, the order of processing is as follows:

1. Calculate sea ice concentrations with atmospheric correction.
2. Apply GR filters.
3. Apply SST mask.
4. Apply land spillover correction.

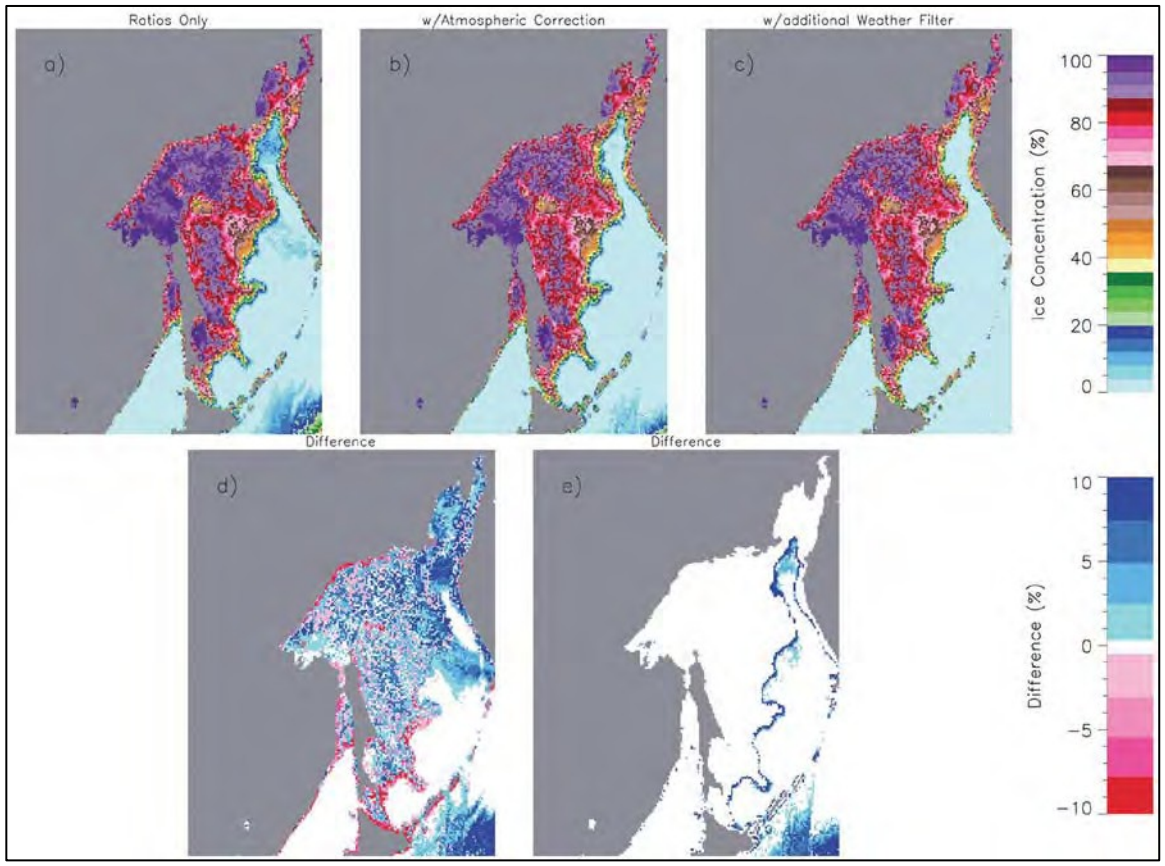

Figure 5. AMSR-E sea ice concentrations for March 1, 2007. (a) Ice concentrations calculated using PRR (19), PRR (89), and ΔGR without applying an atmospheric correction; (b) ice concentration with atmospheric correction; (c) final ice concentration with additional clean-up over the open ocean by applying the standard NASA Team GR weather filters; (d) difference between (a) and (b); (e) difference between (b) and (c). Differences greater than 10% have been truncated for the erroneous sea ice concentrations in the lower right corner.

3.2.2 Snow depth on sea ice

The AMSR-E snow-depth-on-sea-ice algorithm was developed using DMSP SSMI data (Markus and Cavalieri 1998) to estimate snow depth on sea ice from space. The snow depth on sea ice is calculated using the spectral gradient ratio of the 18.7 GHz and 37 GHz vertical polarization channels,

$$h_s = a_1 + a_2 \, GRV(ice) \quad (12)$$

where h_s is the snow depth in meters, and a_1=2.9 and a_2=-782 are coefficients derived from the linear regression of *in situ* snow depth measurements on microwave data. GRV(ice) is the spectral gradient ratio corrected for the sea ice concentration, C, as follows

$$GRV(ice) = [TB(37V)-TB(19V)-k_1(1-C)] / [TB(37V)+TB(19V)-k_2(1-C)] \quad (13)$$

with $k_1=TB_O(37V)-TBO(19V)$ and $k_2=TB_O(37V)+TB_O(19V)$. The open water brightness temperatures, TB_O, are average values from open ocean areas and are used as constants. The principal idea of the algorithm is similar to the AMSR-E snow-on-land algorithm (Kelly et al. 2003) utilizing the assumptions that scattering increases with increasing snow depth and that the scattering efficiency is greater at 37 GHz than at 19 GHz. For snow-free sea ice, the gradient ratio is close to zero and it becomes more and more negative as the snow depth (and grain size) increases. The correlation of regional *in situ* snow depth distributions and satellite-derived snow depth distributions is 0.81 (Figure 6). The upper limit for snow depth retrievals is 50 cm, which is a result of the limited penetration depth a 19 and 37 GHz.

The algorithm is applicable to dry snow conditions only. At the onset of melt, the emissivity of both the 19 GHz and the 37 GHz channels approach unity (that of a blackbody) and the gradient ratio approaches zero initially before becoming positive. Thus, snow depth is indeterminate under wet snow conditions. Snow, which is wet during the day, frequently refreezes during the night. This refreezing results in very large grain sizes (Colbeck 1982) which leads to a reduced emissivity at 37 GHz relative to 19 GHz thereby decreasing GRV(ice) and thus leads to an overestimate of snow depth. These thaw-freeze events, therefore, cause large temporal variations in the snow depth retrievals. This temporal information is used in the algorithm to flag the snow depths as unretrievable from those periods with large fluctuations.

As grain size *in situ* measurements are even less frequently collected than snow depth measurements, the influence of grain size variations could not be incorporated into the algorithm. Because of the uncertainties in grain size and density variations as well as sporadic weather effects, AMSR-E snow depth products will be 5-day averages similar to the snow-on-land product.

Snow depths are retrieved for the entire Southern Ocean, but only for the seasonal sea ice zones in the Arctic, because the microwave signature of snow is very similar to the multiyear ice signature so that snow depth on multiyear ice cannot be retrieved unambiguously. To this end, we use a dynamic multiyear ice mask based on a threshold in GR which evolves on a day-to-day basis starting from October 1 of each year until the onset of melt.

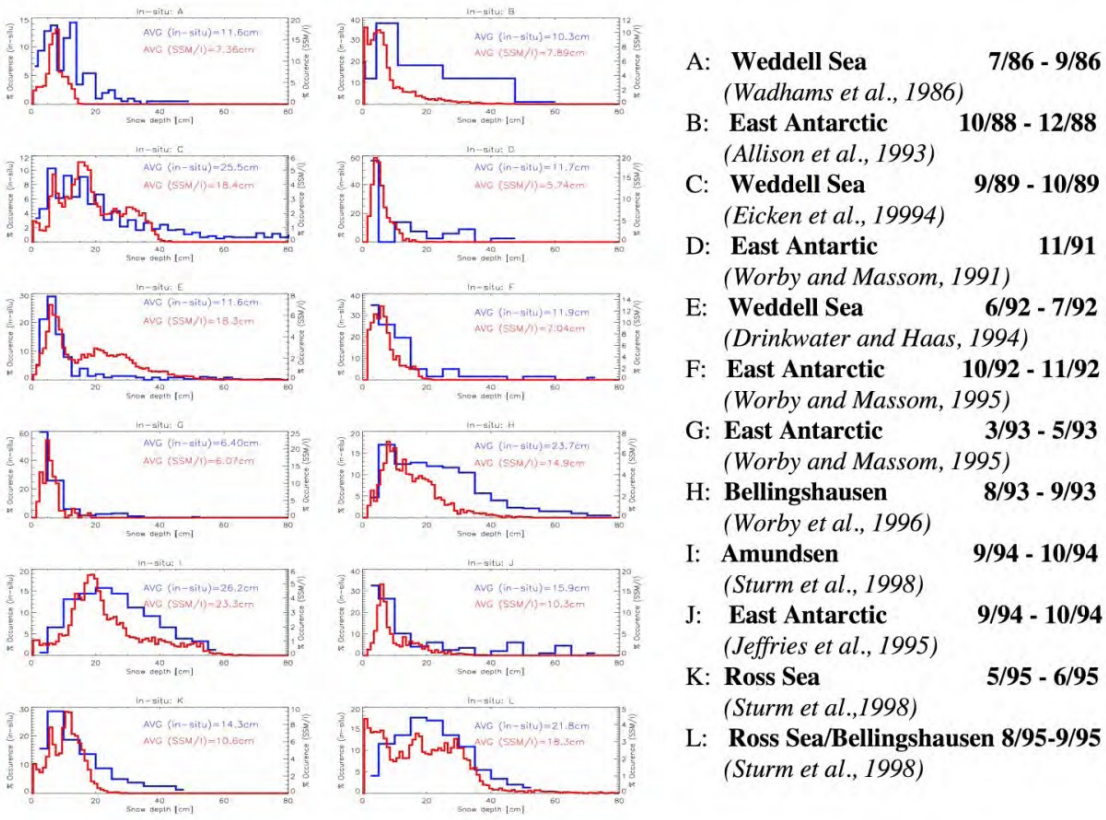

A: **Weddell Sea** **7/86 - 9/86**
(Wadhams et al., 1986)
B: **East Antarctic** **10/88 - 12/88**
(Allison et al., 1993)
C: **Weddell Sea** **9/89 - 10/89**
(Eicken et al., 19994)
D: **East Antartic** **11/91**
(Worby and Massom, 1991)
E: **Weddell Sea** **6/92 - 7/92**
(Drinkwater and Haas, 1994)
F: **East Antarctic** **10/92 - 11/92**
(Worby and Massom, 1995)
G: **East Antarctic** **3/93 - 5/93**
(Worby and Massom, 1995)
H: **Bellingshausen** **8/93 - 9/93**
(Worby et al., 1996)
I: **Amundsen** **9/94 - 10/94**
(Sturm et al., 1998)
J: **East Antarctic** **9/94 - 10/94**
(Jeffries et al., 1995)
K: **Ross Sea** **5/95 - 6/95**
(Sturm et al.,1998)
L: **Ross Sea/Bellingshausen 8/95-9/95**
(Sturm et al., 1998)

Figure 6: Comparison of in-situ and SSM/I-derived snow depth distributions [from Markus and Cavalieri 1998].

3.2.3 Sea ice drift

The method to estimate sea ice drift is the Maximum Cross-Correlation feature-tracking algorithm developed at the University of Colorado (CU) (Emery et al., 1995). The basic methodology of the algorithm is fairly simple. Two spatially coincident images are obtained, separated by some period of time. A target area, which may be defined by a pixel or a group of pixels, is chosen in the first (older) image. Then, a search area surrounding the target area is chosen in the second (newer) image (Figure 1). Correlations with the target area in the first image are compared with all regions (of the target area's size) in the search area in the second image. The region with the highest correlation is determined to be the location where the

target moved (Figure 2). A filtering algorithm is then employed to remove at least some of the questionable matches.

Gridded Level 3 daily composite brightness temperatures at 12.5 km on the polar stereographic grid are used as input into the motion algorithm. Ice motions are calculated from two composite images using the sliding window to find the correlation peak, which determines the distance a feature has moved. The drift is then computed by dividing the distance by the time separation (24 hours). A sea ice mask is applied to only retrieve ice motion where concentration is above the standard sea ice extent threshold of 15% concentration. False correlations can occur due to clouds or variability of ice surface features. To eliminate this, first a minimum correlation threshold of 0.7 is applied to eliminate weak matches. Next a post-processing filter program is run to remove at least some questionable and erroneous motions. This uses the fact that motion is highly spatially correlated and requires that each vector be reasonably consistent in speed and direction with at least two neighboring motion estimates.

The CU algorithm is simple to implement and widely validated. It has been widely used on a variety of imagery, including AMSR-E (e.g., Meier and Dai 2006) and is currently the basis for a long-term sea ice drift product (Tschudi et al. 2016) at the National Snow and Ice Data Center. In theory the accuracy of the algorithm is limited by the gridded spatial resolution of the input data – i.e., a sea ice parcel either stays in its current grid cell or moves to a surrounding grid cell. This would limit the accuracy to ~12.5 km per day. There are also additional error sources such as false correlations from clouds or ice surface changes, so the uncertainty would be even more than 12.5 km per day. However, the algorithm includes a 4X oversampling routine to yield a theoretical accuracy of up to 3.125 km per day. Validation studies of AMSR-E motions in comparison with buoy-derived motions (Meier and Dai 2006) show an RMS error of 4.5 – 5.0 km per day for each velocity component with negligible bias. This is consistent with previous studies using SSMI-derived motions, given the increased resolution of AMSR-E (Meier et al., 2000). Errors are lowest in the central ice pack during winter. Higher errors occur near the ice edge due to growth and melt of ice and thin ice condition, during summer melt due to liquid water on the surface obscuring possible correlation, and near the coast due to the spatial resolution limitations.

3.2.4 Adjustment of brightness temperatures

As noted above, the sea ice algorithms for AMSR2 are the same as those used for AMSR-E. The only substantial difference is that AMSR2 brightness temperatures are adjusted – i.e., intercalibrated – to match AMSR-E so that the algorithm coefficients can remain the same and obtain consistent geophysical estimates from both AMSR-E and AMSR2.

Most intercalibration efforts use overlap between sensors to make adjustments to the sensor data. This was not possible here because there was no overlap between AMSR2 and the fully-operational AMSR-E. However, AMSR-E did operate in a slow rotation mode. This allowed an intercalibration across common points of AMSR2 and the slow-rotation AMSR-E brightness temperatures. Regressions were performed for these common points over a full year and averaged to develop regression equations to adjust AMSR2 brightness temperatures into "pseudo-AMSR-E" brightness temperatures that would be consistent with the AMSR-E algorithms; regressions were done independently for both the Arctic and the Antarctic. The values used in the AMSR2 processing are provided in Table 1 below. These regression equations are applied to the AMSR2 brightness temperatures before they are fed into the subsequent geophysical algorithms.

Table I

Average regression and correlation coefficients for AMSR2 T_bs, based on comparison with 2 rpm AMSR-E T_bs for January – December 2013 (From Meier and Ivanoff 2017)

	Northern Hemisphere			**Southern Hemisphere**		
Channel	*Slope*	*Intercept*	*Correlation*	*Slope*	*Intercept*	*Correlation*
18V	1.031	-9.710	0.9984	1.032	-10.013	0.9982
18H	1.001	-1.104	0.9985	1.000	-1.320	0.9983
23V	0.999	-1.706	0.9979	0.993	-0.987	0.9976
36V	0.997	-2.610	0.9916	0.995	-2.400	0.9919
36H	0.996	-2.687	0.9938	0.994	-2.415	0.9932
89V	0.989	0.677	0.9766	0.975	4.239	0.9619
89H	0.977	3.184	0.9621	0.969	4.935	0.9549

Overall, the regressions showed very good consistency between AMSR2 and the slow-rotation AMSR-E. The most notable difference is found in the 18 GHz V polarization channel, which has slopes slightly off from 1 and higher intercept values. The 89 GHz channels also show less agreement than the other channels, likely due to the greater atmospheric emission at 89 GHz.

For sea ice, the adjustments are evaluated in terms of minimizing the difference in extent, area, and concentration. This was not explicitly possible here because there is not complete coverage to calculate these parameters from the AMSR-E slow rotation data. In order to examine these

variables, a bridge concentration data set was used, based on SSMIS brightness temperatures. This bridge dataset spanned a full year of AMSR-E and AMSR2 (2010 – 2013). Differences in extent and area between each sensor and SSMIS were calculated. These two fields were then differenced to obtain a double-difference AMSR2-AMSRE extent and area difference. From this, and examination of the concentration fields, it was found that an adjustment in the GR3619 weather filter, from 0.050 to 0.046, was needed to optimize the sea ice concentration fields.

The double-difference fields and subsequent GR3619 adjustment decreased the extent bias between AMSR2 and AMSR-E from ~200,000 square kilometers to <10,000 square kilometers (Figure 7). This is as good or better than previous sea ice extent sensor intercalibrations (e.g., Cavalieri et al. 2012; Meier et al. 2011). The full methodology for deriving the regression coefficients and the adjustment to AMSR2 brightness temperatures for the sea ice algorithms is described in Meier and Ivanoff (2017).

4. Variance and Uncertainty Estimates

The sea ice products have been thoroughly validated in previous studies using AMSR-E (e.g., Markus and Cavalieri 2000; Markus and Cavalieri 2009; Markus and Cavalieri 1998; Liu and Cavalieri 1998). Further comparisons have been made for AMSR2 sea ice concentration in Meier et al. (2017). These compared AMSR2 concentration estimates with concentrations derived from visible imagery obtained from the Suomi Visible and Infrared Imaging Radiometer Suite (VIIRS).

This validation showed a concentration bias of 3.9% and an RMSE of 11.0% in the Arctic (Figure 8), and a bias of 4.45% and an RMSE of 8.8% in the Antarctic. These values are consistent with previous validation studies of AMSR-E sea ice concentrations. There is considerable variation though in the accuracy of AMSR2 concentration, depending on sea ice conditions. Errors are low for high concentration regions, but are higher in regions with lower concentrations, such as the marginal ice zone. Again, this performance is typical for passive microwave retrievals and has been found in numerous other studies.

5. Implementation issues

5.1 Computation/programming/procedural consideration

5.2 Quality control and diagnostics

5.3 Constraints, limitations and diagnostics

The basic limitations of ice concentration data from AMSR2 include relatively coarse resolution and the inability to unambiguously identify areas covered by thin ice, pancake ice and meltponded ice. Thin ice, pancake ice and meltponded ice can have emissivities intermediate to those of open water and dry thick ice and could contribute to significant uncertainties in the retrieval of ice concentration. A good scheme that enables classification of each data element into different surface types would help minimize uncertainties.

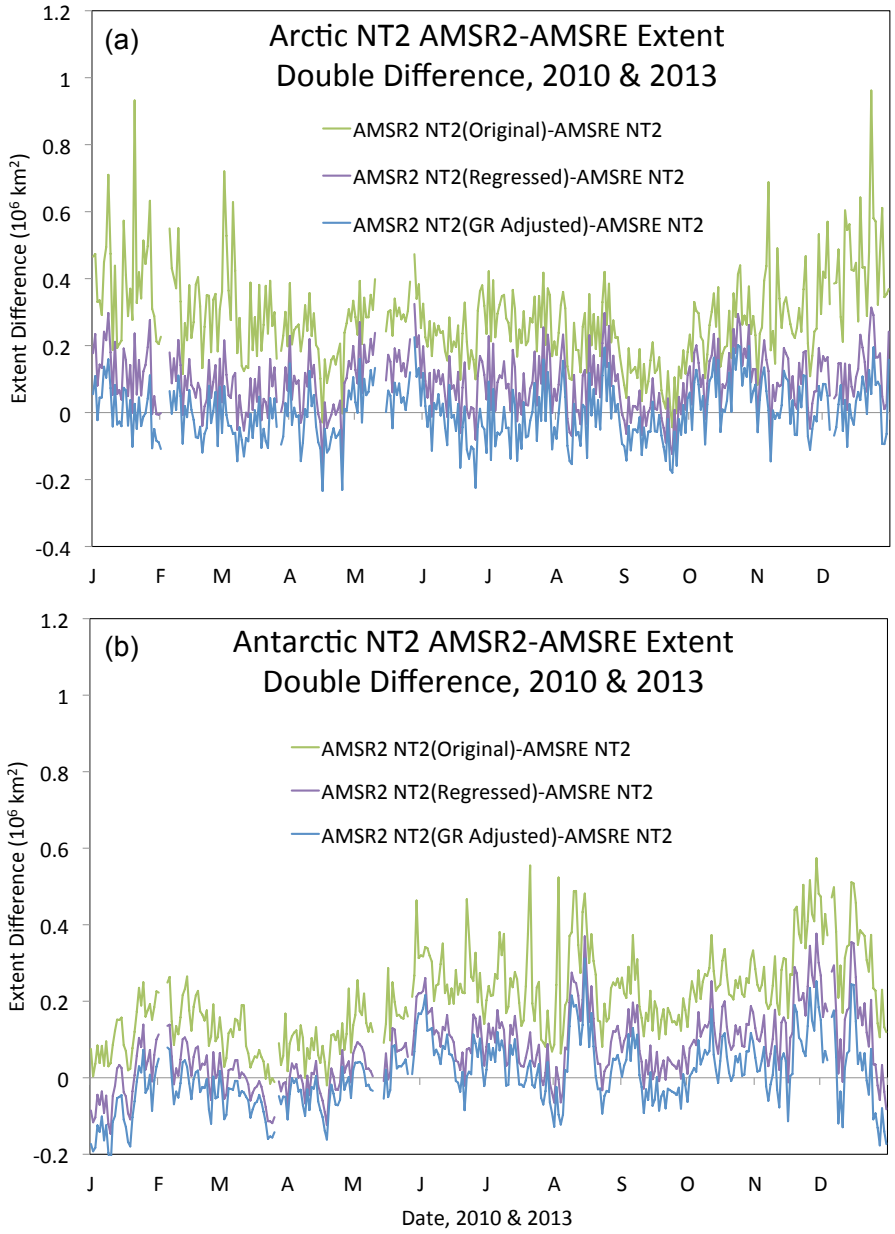

Fig. 7. (a) Arctic and (b) Antarctic extent double differences, (AMSR2 – SSMIS) – (AMSR-E – SSMIS) for original AMSR2 (green), regressed AMSR2 (purple), and regressed AMSR2 with GR adjustment (blue). From Meier and Ivanoff (2017).

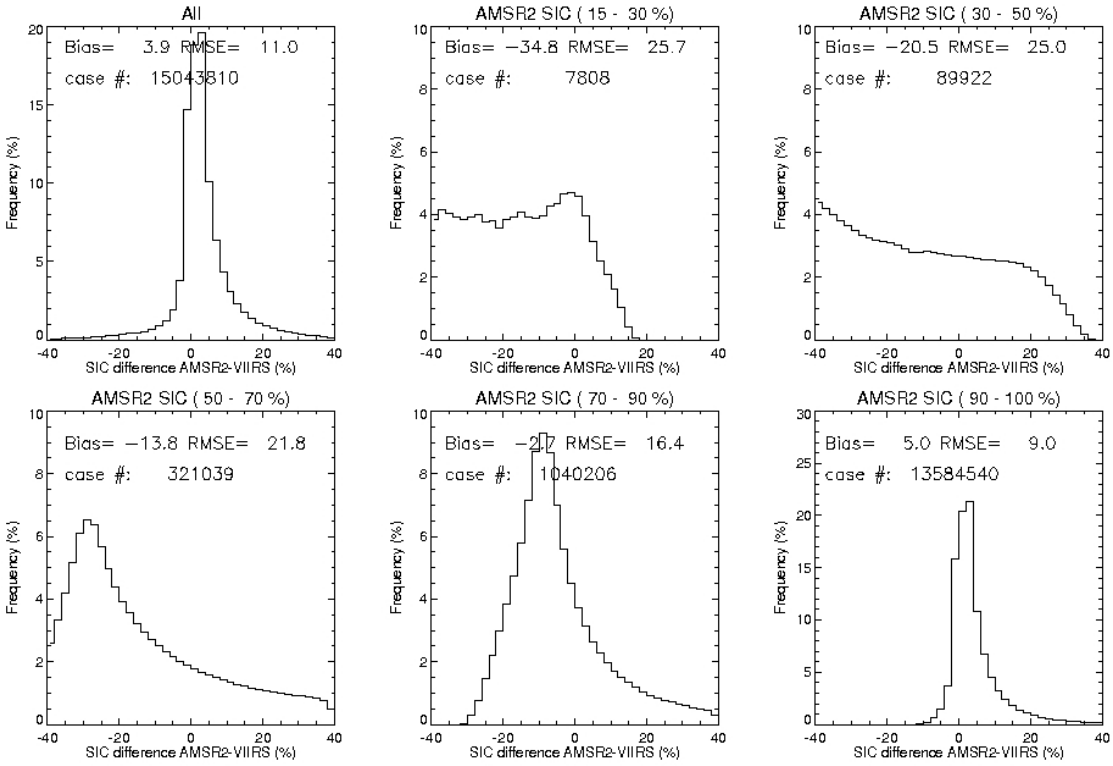

Fig. 8. Comparison of AMSR2 minus VIIRS ice concentrations for different AMSR2 ice concentration ranges/bins in the Arctic. The AMSR2 concentration is computed with the NASA Team 2 algorithm. Note that the y-axis range is different for "All", "90-100%", and the other plots. From Meier et al. (2017).

6. References

Bhatt, U. S., et al. 2010. Circumpolar Arctic tundra vegetation change is linked to sea---ice decline. *Earth Interactions* 14: 1-20. doi:10.1175/2010EI315.1.

Cavalieri, D. J., P. Gloersen, and W. J. Campbell. 1984. Determination of sea ice parameters with the NIMBUS 7 scanning multichannel microwave radiometer. *J. Geophys. Res.* 89: 5355-5369.

Cavalieri, D. J., K. St. Germain, and C. T. Swift. 1995. Reduction of Weather Effects in the Calculation of Sea Ice Concentration with the DMSP SSM/I. *J. Glaciology* 41: 455-464.

Cavalieri, D. J., C. L. Parkinson, P. Gloersen, J. C. Comiso, and H. J. Zwally. 1999. Deriving Long-Term Time Series of Sea Ice Cover from Satellite Passive---Microwave Multisensor Data Sets. *J. Geophys. Res.* 104: 15,803-15,814.

Cavalieri, D. J., C. L. Parkinson, N. DiGirolamo, and A. Ivanoff, 2012. Intersensor calibration between F13 SSMIS and F17 SSMIS for global sea ice data records, *IEEE Geosci. Rem. Sens. Lett.*, vol. 9, no. 2, pp. 233-236, doi:10.1109/LGRS.2011.2166754.

Colbeck, S. C. 1982. An overview of seasonal snow metamorphism. *Rev. Geophys. Space Phys.* 20: 45-61.

Combes, J. M., A. Grossmann, and Ph. Tchamitchian. 1989. Wavelet: time frequency methods and phase space. In *Proceedings of the International Conference on Wavelet, Marseille, France*. New York: Springer-Verlag.

Comiso, J. C., D. J. Cavalieri, C. L. Parkinson, and P. Gloersen. 1997. Passive microwave algorithms for sea ice concentration - A comparison of two techniques. *Remote Sens. Environ.*, 60: 357-384.

Comiso, J. C. 2012. Large decadal decline in the Arctic multiyear ice cover. *J. Climate* 25(4): 1176-1193. doi: 10.1175/JCLI-D-11-00113.1.

Comiso, J. C. and F. Nishio. 2008. Trends in the sea ice cover using enhanced and compatible AMSR-E, SSM/I, and SMMR data. *J. Geophys. Res.* 113(2): C02S07. doi:10.1029/2007JC004257.

Comiso, J. C. 2009. Enhanced sea ice concentration and ice extent from AMSR---E Data. *J. Remote Sensing Soc. of Japan* 29(1): 199---215.

Comiso, J. C., D. J. Cavalieri, and T. Markus. 2003. Sea ice concentration, ice temperature, and snow depth, using AMSR-E data. *IEEE TGRS* 41(2): 243---252.

Comiso, J. C. 2010. *Polar Oceans from Space*. New York: Springerverlag.

Comiso, J. C. 1986. Characteristics of winter sea ice from satellite multispectral microwave observations. *J. Geophys. Rev.* 91(C1): 975-994.

Comiso, J. C. and K. Steffen. 2001. Studies of Antarctic sea ice concentrations from satellite data and their applications. *J. Geophys. Res.* 106(C12): 31361-31385.

Comiso, J. C. and C. L. Parkinson. 2008. Arctic sea ice parameters from AMSR-E using two techniques, and comparisons with sea ice from SSM/I. *J. Geophys. Res.* 113(C2): C02S05. doi:10.1029/2007JC004255.

Comiso, J. C. 1995. *SSM/I Concentrations using the Bootstrap Algorithm*. NASA RP 1380. Goddard Space Flight Center: National Aeronautics and Space Administration.

Emery, W., C. Fowler, and J. Maslanik. 1995. Satellite Remote Sensing of Ice Motion, in *Oceanographic Applications of Remote Sensing*, ed. Motoyoshi Ikeda and Frederic W. Dobson. CRC Press, Boca Raton.

Fraser R. S., N. E. Gaut, E. C. Reifenstein, and H. Sievering. 1975. Interaction Mechanisms------ Within the Atmosphere. In *Manual of Remote Sensing* edited by R. G. Reeves, A. Anson, D. Landen, 181-223. Falls Church, VA: American Society of Photogrammetry.

Gloersen, P. and D. J. Cavalieri. 1986. Reduction of weather effects in the calculation of sea ice concentration from microwave radiances. *J. Geophys. Res.* 91: 3913-3919.

Kelly, R. E. J, A. T. C. Chang, L. Tsang, and J. L. Foster. 2003. A prototype AMSR---E global snow area and snow depth algorithm. *IEEE Transactions on Geoscience and Remote Sensing* 41(2): 230-242.

Kummerow, C. 1993. On the accuracy of the Eddington approximation for radiative transfer in the microwave frequencies. *J. Geophys. Res.* 98: 2757-2765.

Lindsay, R. W. and J. Zhang. 2005. The thinning of Arctic sea ice, 1988-2003: Have we reached the tipping point? *J. Climate* 18: 4879-4894.

Markus, T. and D. J. Cavalieri. 1998. Snow depth distribution over sea ice in the Southern Ocean from satellite passive microwave data. In *Antarctic Sea Ice: Physical Processes, Interactions and Variability*, 19-39. Washington, DC: American Geophysical Union.

Markus, T. and D. J. Cavalieri. 2000. An enhancement of the NASA Team sea ice algorithm. *IEEE Trans. Geosci. and Remote Sensing* 38:1387-1398.

Markus, T. and D. J. Cavalieri. 2009. The AMSR---E NT2 sea ice concentration algorithm: its basis and implementation. *Journal of The Remote Sensing Society of Japan* 29(1): 216-225.

Markus, T. and S. T. Dokken. 2002. Evaluation of Arctic late summer passive microwave sea ice retrievals. *IEEE Trans. Geoscience Remote Sensing* 40(2): 348-356.

Matzler, C., R. O. Ramseier, and E. Svendsen. 1984. Polarization effects in sea---ice signatures. *IEEE J. Oceanic Eng.* 9: 333-338.

Meier, W. N., J. A. Maslanik, and C. W. Fowler. 2000. Error analysis and assimilation of remotely sensed ice motion within an Arctic sea ice model, J. Geophys. Res., 105(C2), 3339–3356, doi:10.1029/1999JC900268.

Meier, W.N., and M. Dai. 2006. High-resolution sea-ice motions from AMSR-E imagery, *Ann. Glaciol.*, 44, 352-356.

Meier, W. N., S. J. S. Khalsa, and M. H. Savoie. 2011. Intersensor calibration between F-13 SSM/I and F-17 SSMIS near-real-time sea ice estimates. *IEEE Trans. Geosci. Rem. Sens.*, vol. 49, no. 9, pp. 3343-3349.

Parkinson, C. L. and J. C. Comiso. 2008. Antarctic sea ice from AMSR---E from two algorithms and comparisons with sea ice from SSM/I. *J. Geophys. Res.* 113(C2): C02S06. doi:10.1029/2007JC004253.

Shibata, A., H. Murakami, and J. Comiso. 2010. Anomalous Warming in the Arctic Ocean in the Summer of 2007. *J. Remote Sensing Society of Japan* 30(2): 105-113.

Sigmond, M. and J. C. Fyfe. 2010. Has the ozone hole contributed to increased Antarctic sea ice extent? *Geophys. Res. Lett.* 37(L18): L18502. doi:10.1029/2010GL044301.

Svendsen, E., C. Matzler, and T.C. Grenfell. 1987. A model for retrieving total sea ice concentration from a spaceborne dual-plarized passive microwave instrument operating near 90 GHz. *Int. J. Rem. Sens.* 8: 1479-1487.

Swift, C. T., L. S. Fedor, and R. O. Ramseier. 1985. An algorithm to measure sea ice concentration with microwave radiometers. *J. Geophys. Res.* 90(C1): 1087-1099.

Tschudi, M., C. Fowler, J. Maslanik, J. S. Stewart, and W. Meier. 2016. *Polar Pathfinder Daily 25 km EASE-Grid Sea Ice Motion Vectors, Version 3*. Boulder, Colorado USA. NASA National Snow and Ice Data Center Distributed Active Archive Center. doi: http://dx.doi.org/10.5067/O57VAIT2AYYY.

Turner, J., J. C. Comiso, G. J. Marshall, T. A. Lachlan---Cope, T. Bracegirdle, T. Maksym, M. Meredith, and Z. Wang. 2009. Non---annular atmospheric circulation change induced by stratospheric ozone depletion and its role in the recent increase of Antarctic sea ice extent. *Geophy. Res. Lett.* 36(L8): L08502. doi:10.1029/2009GL037524.

Wang, M. and J. Overland. 2009. A sea ice free summer Arctic within 30 years? *Geophys. Res.Lett.* 36(L7): L07502. doi:10.1029/2009GL037820.

Yaguchi, R. and K. Cho. 2009. Validation of sea ice drift vector extraction from AMSR---E and SSM/I data using MODIS data. *J. Remote Sens. Japan* 29(1): 242-252.

Zwally, H. J., J. C. Comiso, C. Parkinson, D. Cavalieri, P. Gloersen. 2002. Variability of the Antarctic sea ice cover. *J. Geophys. Res.* 107(C5): 1029-1047.

Zwally, H. J., J. C. Comiso, C. L. Parkinson, W. J. Campbell, F. D. Carsey, and P. Gloersen. 1983. Antarctic Sea Ice 1973---1976 from Satellite Passive Microwave Observations. *NASA Spec. Publ.* 459. Washington, DC: NASA.